Check for updates

Improved subsalt images with least-squares reverse time migration

Ping Wang[1], Shouting Huang[1], and Ming Wang[1]

Abstract

Complex overburdens often distort reservoir images in terms of structural positioning, stratigraphic resolution, and amplitude fidelity. One prime example of a complex overburden is in the deepwater Gulf of Mexico, where thick and irregular layers of remobilized (i.e., allochthonous) salt are situated above prospective reservoir intervals. The highly variant salt layers create large lateral velocity variations that distort wave propagation and the illumination of deeper reservoir targets. In subsalt imaging, tools such as reflection tomography, full-waveform inversion, and detailed salt interpretation are needed to derive a high-resolution velocity model that captures the lateral velocity variations. Once a velocity field is obtained, reverse time migration (RTM) can be applied to restore structural positioning of events below and around the salt. However, RTM by nature is unable to fully recover the reflectivity for desired amplitudes and resolution. This shortcoming is well-recognized by the imaging community, and it has propelled the emergence of least-squares RTM (LSRTM) in recent years. We have investigated how current LSRTM methods perform on subsalt images. First, we compared the formulation of data-domain versus image-domain least-squares migration, as well as methods using single-iteration approximation versus iterative inversion. Then, we examined the resulting subsalt images of several LSRTM methods applied on the synthetic and field data. Among our tests, we found that image-domain single-iteration LSRTM methods, including an extension of an approximate inverse Hessian method in the curvelet domain, not only compensated for amplitude loss due to poor illumination caused by complex salt bodies, but it also produced subsalt images with fewer migration artifacts in the field data. In contrast, an iterative inversion method showed its potential for broadening the bandwidth in the subsalt, but it was less effective in reducing migration artifacts and noise. Based on our understanding, we evaluated the current state of LSRTM for subsalt imaging.

Introduction

We can consider recorded seismic data to be the result of forward-modeling experiments through subsurface structures. To image the reflectivity of the subsurface, we need to reverse the effects of the forward wave propagation. In other words, we need to apply an inverse of the forward-modeling operator on the recorded data to obtain the desired reflectivity. The exact inverse is difficult to obtain and is therefore approximated in all standard migration algorithms, such as Kirchhoff migration and reverse time migration (RTM). For subsalt imaging, in which the presence of large velocity contrasts and steep dips is common, RTM has become the migration method of choice. RTM approximates the inverse of the forward wave propagation with an adjoint operation that forms the image from a combination of the forward-propagated source wavefield and the backward-propagated receiver wavefield (Baysal et al., 1983; Etgen et al., 2009; Zhang and Zhang, 2009). The accuracy of the approximation can be negatively impacted by spatial aliasing, limited aperture, and noise in the input data, as well as by nonuniform illumination due to a complex overburden (Claerbout, 1992). As a result, RTM images may contain migration artifacts with limited bandwidth and uneven amplitudes. For example, Figure 1a shows a cross section of the zero-angle reflectivity image computed from the SEG SEAM I model in which the amplitude along each subsalt horizon is uniform. However, the RTM image in Figure 1b shows amplitude dimming in the lower circle due to illumination loss caused by the overburden salt body and migration artifacts in the upper circle likely due to sparse shot sampling and irregular illumination. Overall, the resulting RTM image does not perfectly resemble the original reflectivity model (Figure 1a), particularly in the subsalt region. The deviation is due to the approximation made in the inverse of the forward-modeling operator. The approximation error increases with structural complexity and thus tends to produce larger deviations in the subsalt region.

Least-squares migration (LSM) was proposed to improve the approximation of the inverse of the forward-modeling operator through either an iterative inversion (Tarantola, 1987; Schuster, 1993; Nemeth et al., 1999) or a single-iteration inversion (Hu et al., 2001; Rickett,

[1]CGG, Houston, Texas, USA. E-mail: ping.wang@cgg.com; shouting.huang@cgg.com; merlin.wang@cgg.com.

Manuscript received by the Editor 7 November 2016; revised manuscript received 4 March 2017; published ahead of production 10 May 2017; published online 19 June 2017. This paper appears in *Interpretation*, Vol. 5, No. 3 (August 2017); p. SN25–SN32, 6 FIGS., 1 TABLE.
http://dx.doi.org/10.1190/INT-2016-0203.1. © 2017 Society of Exploration Geophysicists and American Association of Petroleum Geologists. All rights reserved.

2003; Guitton, 2004; Lecomte, 2008). In recent years, least-squares RTM (LSRTM) has attracted considerable attention. The often-cited benefits of LSRTM include more correct image amplitudes due to the ability to compensate for illumination loss caused by overburden and acquisition effects, more coherent images due to the ability to reduce migration artifacts, and higher image resolution (vertically and laterally) due to the ability to remove the source signature and source/receiver ghost, as well as migration stretch (Wong et al., 2011; Dong et al., 2012; Dai et al., 2013; Zhang et al., 2013; Zeng et al., 2014). Not surprisingly, LSRTM is being recognized as the next-generation technology for subsalt imaging in the deepwater Gulf of Mexico (GOM).

Theory

In this section, we discuss the general theory of LSM that is applicable to commonly used migration methods, including RTM. We also compare how different LSM methods invert the Hessian matrix (Table 1) appearing in the inversion formula. The Hessian matrix is a square matrix of the second-order derivatives of the objective function with respect to the reflectivity model. Because the Hessian matrix is closely related to the seismic resolution and illumination of the subsurface, computing the inverse of the Hessian matrix is the key to LSM in terms of illumination compensation, noise (migration artifacts) reduction, and resolution enhancement. After discussion of existing iterative and single-iteration LSM methods, we outline an image-domain single-iteration LSM implementation in the curvelet domain.

LSM (Tarantola, 1987) inverts for a reflectivity model m to fit the recorded data d_0

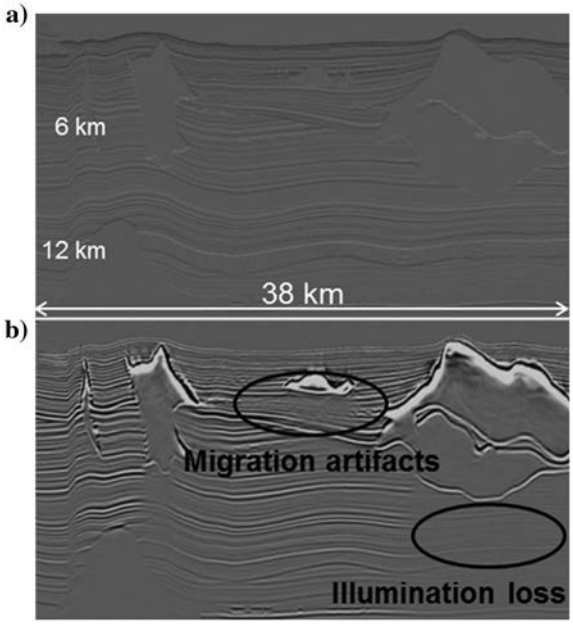

Figure 1. SEAM I synthetic study: (a) reflectivity section of the SEAM I model and (b) RTM stack image.

$$f(m) = \frac{1}{2}\|d_0 - Lm\|^2, \tag{1}$$

where f is the cost function to be minimized and L is the linearized Born modeling operator or demigration operator. If L^TL is invertible, the least-squares solution for equation 1 can be written as

$$m = (L^TL)^{-1}L^Td_0, \tag{2}$$

where L^T is the migration operator and L^TL is the so-called Hessian matrix H. The key to LSM is to obtain the inverse of H; however, the computation and storage of H are not feasible for real 3D problems. Alternatively, different approximate solutions, such as gradient-based iterative approaches (Schuster, 1993; Nemeth et al., 1999; Tang, 2008) and single-iteration approaches (Hu et al., 2001; Rickett, 2003; Guitton, 2004; Lecomte, 2008), have been pursued.

Iterative least-squares migration

Regardless of the invertibility of H, equation 1 can be iteratively solved by either steepest descent or conjugate gradient methods and the gradient can be written as

$$g = L^T(d_0 - Lm). \tag{3}$$

For one iteration of LSM, the computation of g in equation 3 costs one Born modeling (i.e., demigration) and one migration. If more than 10 iterations are needed for convergence, the costs of data-domain iterative LSM are at a level of more than 20 migrations (part of the computation for Born modeling and migration may be shared to save some costs). This can be computationally prohibitive for modern 3D marine streamer data that use RTM extensively for model building as well as for final migrations that compute images with moderate to high frequency.

Single-iteration least-squares migration

As discussed above, direct (equation 2) or iterative (equation 3) inversion methods are either impractical or expensive. The cost-reducing alternative is to approximate the Hessian matrix in a single iteration. Lecomte (2008) and Fletcher et al. (2016) propose to obtain the Hessian matrix using point spread functions (PSFs). The PSF method computes the impulse response (Hessian) on a coarse grid (to reduce interference between PSFs) of scattered points. The Hessian for every image point is then obtained by interpolating between computed PSFs. LSM results are achieved by deconvolving computed PSFs from the raw migration image.

Guitton (2004) proposes to use nonstationary matching filters to approximate the inverse of the Hessian matrix in one iteration. In Guitton's approach, Born modeling is first performed using the raw migration

image m_0 and the existing velocity field to derive synthetic data $d_1 = Lm_0$, which is then remigrated to obtain a new image:

$$m_1 = L^T L m_0. \tag{4}$$

Next, nonstationary matching filters (or inverse Hessian filters) F are found by minimizing the following cost function:

$$f(F) = \frac{1}{2}\|m_0 - Fm_1\|^2. \tag{5}$$

After obtaining F, the image-domain single-iteration LSM image can be written as

$$m = Fm_0. \tag{6}$$

Guitton (2004) computes multicoefficient matching filters in the spatial domain (Rickett et al., 2001). However, different events may have different illumination patterns. Therefore, it is desirable to decompose the input image for more accurate derivation of inverse Hessian filters.

Curvelet-domain Hessian filter

The curvelet transform decomposes seismic events into different orientations and frequency scales. Using the curvelet transform, we can extend the idea of a guided image filter proposed by He et al. (2013) to formulate a curvelet-domain Hessian filter (CHF). The cost function of the image-domain CHF can be written as

$$f(s) = \|C(m_0) - sC(m_1)\|^2 + \epsilon\|s\|^2, \tag{7}$$

where C is the curvelet transform operator, s is the matching filter, and ϵ is a weighting factor for the Tikhonov regularization. The final output image is

$$m = C^{-1}(|s|C(m_0)), \tag{8}$$

where C^{-1} is the inverse curvelet transform operator and $|\,|$ is used to remove the phase and make the matching filter a zero-phase filter.

To compensate for offset-dependent illumination patterns, we further extend CHF to surface-offset gathers (SOGs) (Giboli et al., 2012):

$$f(s^{\text{sog}}) = \|C(m_0) - s^{\text{sog}}C(m_1^{\text{sog}})\|^2 + \epsilon\|s^{\text{sog}}\|^2, \tag{9}$$

$$m^{\text{sog}} = C^{-1}(|s^{\text{sog}}|C(m_0^{\text{sog}})). \tag{10}$$

Here, the same raw stacked image (m_0) is used to design the guided filter for each offset class. We note that the zero-phase filter is important for retaining event curvatures.

In summary, the key to LSM is to obtain an effective inverse of the Hessian matrix. LSM can be formulated either in the data domain, where the least-squares fitting is performed on recorded unmigrated data, or in the image domain, where least-squares fitting is performed on the migrated image. Because a direct inversion is not practical and iterative inversion is expensive, approximation of the Hessian matrix from a single iteration of Born modeling and migration becomes attractive. Similar to the iterative approach, single-iteration LSM can also be implemented in either the data or image domain. Among image-domain single-iteration LSM methods, PSF (Lecomte, 2008; Fletcher et al., 2016) and matching filters (Guitton, 2004) are two current approaches. We proposed the CHF scheme that incorporates a curvelet transform into the matching filter method to better separate events in terms of structural dip and frequency. In addition, we extended CHF from

Table 1. Comparison of different LSM methods: d_0 is the recorded data, m_0 is the raw migration image, L^T is the migration operator, L is the Born modeling operator, C is the curvelet transform operator, and C^{-1} is the inverse curvelet transform operator.

Domain	Approximate inverse Hessian method	Theory	No. of iterations
Data domain	Iterative	Cost objective: $\frac{1}{2}\|d_0 - Lm\|^2$; gradient: $g_i = L^T(d_0 - Lm_i)$ Output image: $m_{i+1} = m_i + \alpha_i g_i$	>10
	CHF (single iteration)	Migration/modeling: $d_1 = LL^T d_0$ Cost objective: $\|C(d_0) - sC(d_1)\|^2 + \epsilon\|s\|^2$ Output image: $m = L^T C^{-1}(\|s\|C(d_0))$	1
Image domain	Iterative	Cost objective: $\frac{1}{2}\|m_0 - L^T Lm\|^2$; gradient: $g_i = L^T L(m_0 - L^T Lm_i)$ Output image: $m_{i+1} = m_i + \alpha_i g_i$	>10
	PSF deconvolution (single iteration)	Modeling/migration: $m_1 = L^T Lm'$ (m': point diffractors model) Output image: $m = \frac{m_0 m_1^*}{m_1 m_1^* + \epsilon}$	1
	CHF (single iteration)	Modeling/migration: $m_1 = L^T Lm_0$ Cost objective: $\|C(m_0) - sC(m_1)\|^2 + \epsilon\|s\|^2$ Output image: $m = C^{-1}(\|s\|C(m_0))$	1

the migrated stack to SOGs to deal with offset-dependent illumination patterns.

Application to the SEG SEAM I synthetic data

One of the main benefits of LSRTM is its ability to compensate for illumination loss and produce amplitudes closer to the true reflectivity than standard RTM does. Using the SEAM I synthetic data, we examine the illumination compensation effects on stacked images generated from data-domain iterative LSRTM (hereafter, "data domain" is omitted), PSF deconvolution, and SOG-based CHF (hereafter, "SOG-based" is omitted). In addition, SOGs from raw RTM and those after CHF are compared to gauge the amplitude compensation for common-image gathers.

The SEAM I model contains realistic velocity/density contrasts with complex salt geometries that create a variety of subsalt illumination issues. It is an ideal synthetic data set for our initial evaluation of different LSRTM algorithms. To avoid the "inverse crime" (the same modeling engine used for input and LSRTM), we modeled the input data using acoustic full-wave modeling instead of acoustic Born modeling, the modeling engine of all the LSRTM algorithms in this study. The modeling frequency is 10 Hz, the shot grid is 150×150 m, whereas the receiver grid is 100×100 m, and the maximum offset is 8 km in inline and crossline directions. For simplicity, we used the true velocity model and synthetic input data without surface multiples or added noise.

Figure 2a shows the raw RTM stack and Figure 2b shows the RTM stack after 20 iterations of iterative LSRTM. Figure 2c and 2d shows the images after single-iteration LSRTM: PSF deconvolution and CHF, respectively. Overall, all three LSRTM methods produced similar stacks (Figure 2b–2d) with visually balanced amplitudes in the subsalt. To quantify the amplitude restoration of different approaches, in Figure 2e, we compared the corresponding amplitude decay curves extracted from Figure 2a to 2d with the true reflectivity (Figure 1a: convolving with the 10 Hz wavelet used to compute the input data). While raw RTM gave relatively weaker amplitudes at deeper depths due to uncompensated illumination loss, all three LSRTM methods produced similar amplitude decay curves as compared with the ground truth.

In the raw RTM SOGs (Figure 3a), we observe that the gathers on the left side have weak amplitudes at near offsets but normal amplitudes at mid and far offsets. This is due to the wavefields or raypaths contributing to the near offsets traveling through a small salt body in the overburden, whereas the raypaths of mid to far offsets undershoot the small salt body. This is not the case for the gathers on the right, which contain weak amplitudes across all offsets due to illumination loss from a much larger overburden salt body. As expected from LSRTM, gathers after CHF (Figure 3b) show better balanced amplitudes across offsets as well as gather groups.

From these SEAM I subsalt synthetic LSRTM tests, we have the following summary:

1) All three LSRTM methods — iterative LSRTM, PSF, and CHF — produced similar stack images and subsalt amplitude decay curves (Figure 2e) that matched the decay curve of the reflectivity model (the ground truth). However, under closer inspection, none of the three methods recovered events that are completely missing (the red arrow in Figure 2a) on the raw RTM stack. Such events have very low or no illumination from the given acquisition and, therefore, cannot be modeled through the Born modeling and restored by LSRTM.

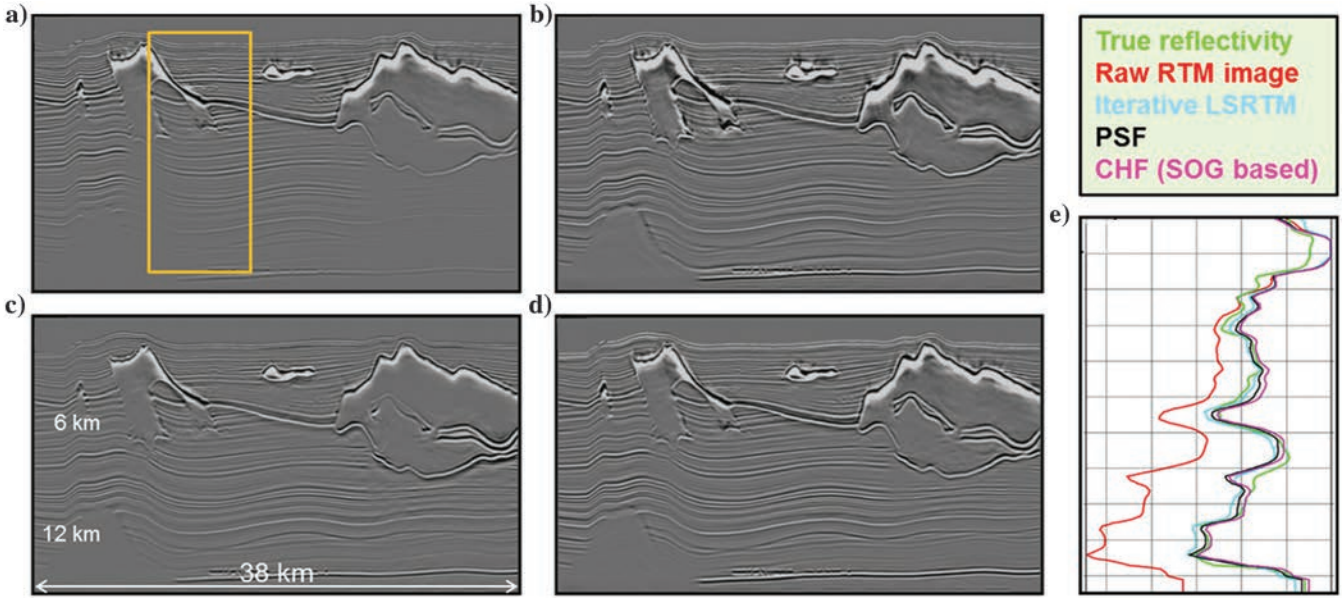

Figure 2. SEAM I synthetic study: (a) RTM image using the forward-modeled synthetic data, (b) iterative LSRTM image, (c) PSF deconvolution image, (d) CHF image, and (e) amplitude decay curves (orange box in [a]) for images in Figures 1a and 2a–2d.

2) Iterative LSRTM produced results comparable with those from the two single-iteration methods after approximately 20 iterations. This is consistent with Guitton's (2004) conclusion that a single-iteration LSRTM is a cost-effective alternative to iterative inversion.
3) As proposed by Fletcher et al. (2016), we computed multiple PSFs of interleaving grids to improve spatial sampling for interpolation while ensuring sufficient isolation of PSFs. This scheme was effective but decreased the efficiency of the PSF approach. We also used salt damping to minimize deconvolution instability around salt bodies. Furthermore, we found that a reweighting-based sparse deconvolution can be used to control noise (Sacchi, 1997).
4) In addition to its computational efficiency, CHF is appealing because it extends the illumination compensation from stack to SOGs, which potentially can be used for amplitude variation with offset analysis and velocity model building.

We note that this test is not completely realistic because we did not include surface-related multiples or noise in the synthetic data and we used the correct velocity model for the test. The reality and possibilities of LSRTM for subsalt imaging would be better answered using field data in a more realistic context, i.e., with an inevitably inaccurate velocity model and abundant noise from residual multiples.

GOM field data example

A wide-azimuth streamer data set from the Keathley Canyon area of the GOM was selected for the field data test. Although the area is known for well-defined salt geometries and overall good data quality, subsalt images in this region still suffer from uneven illumination, visible migration artifacts, and suboptimal resolution. The input data underwent typical preprocessing to remove noise, ghost energy, multiples, etc.

When compared with the raw RTM image (Figure 4a), iterative LSRTM (Figure 4b) produced more continuous subsalt events, particularly within the white circle in Figure 4a. Similar to the results of the synthetic test, subsalt amplitudes in the field data are also more uniform after LSRTM. The resolution of the subsalt region in Figure 4b appears to be higher than the raw RTM stack (Figure 4a). However, part of the higher resolution in the iterative LSRTM comes from boosted noise content and migration artifacts that are likely caused by overfitting of some events that were present in the input data but cannot be correctly modeled by acoustic Born modeling. We stopped the test at the 10th iteration despite the presence of primary signal still in the data residual because the noise level was increasing with the number of iterations.

The CHF image (Figure 4c) also shows balanced amplitudes and more continuous events in the subsalt. Unlike the iterative LSRTM, CHF did not noticeably alter the vertical resolution or frequency content. This is because we did not model the ghost when generating the demigration/migration image because the input had been deghosted, and we used a spiky source wavelet for demigration and migration. As a result, the demi-

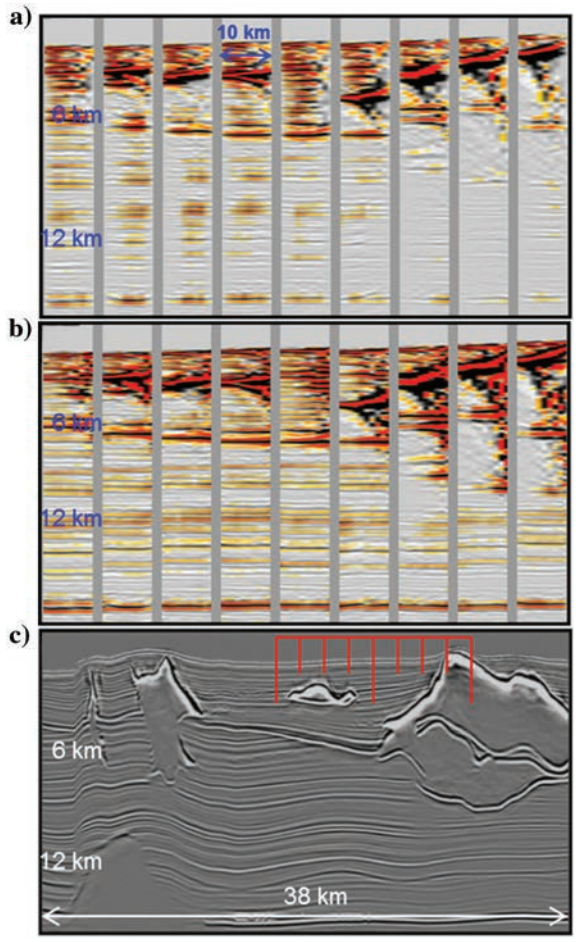

Figure 3. SEAM I synthetic study: (a) raw RTM surface-offset gathers, (b) LSRTM-CHF surface-offset gathers, and (c) LSRTM-CHF stacked image. The red lines in (c) mark the gather locations in (a and b).

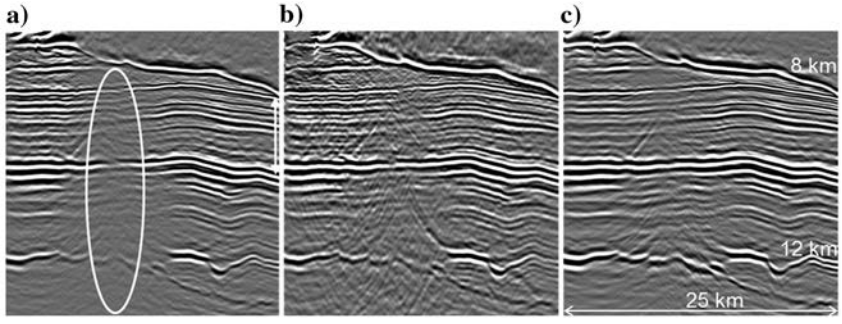

Figure 4. GOM field data example: (a) raw RTM image, (b) iterative LSRTM image, and (c) CHF image. The white circle marks a weak amplitude zone due to illumination loss, and the white arrow marks the prospective Lower Tertiary interval.

gration/migration image (m_1) has frequency content similar to the raw RTM image (m_0). In addition, the design of CHF discourages overboosting of frequency content with a low signal-to-noise ratio (S/N) in the raw RTM image. Alternatively, one can use a band-limited source wavelet (not necessarily a true one) instead of a spiky one in Born modeling and subsequent migration to broaden the bandwidth through wavelet deconvolution. However, if the S/N is low, using a band-limited wavelet will inevitably boost noise as well.

The quality of subsalt images is judged by many factors, such as S/N, event and structural coherency, amplitude consistency, and resolution. Within the prospective Lower Tertiary interval (denoted by the white up-down arrows in Figure 4a), CHF performed better in terms of noise suppression, whereas the iterative method yielded higher resolution but an increased noise level. Both methods were effective at balancing uneven amplitudes in the subsalt, as was also shown in the synthetic test.

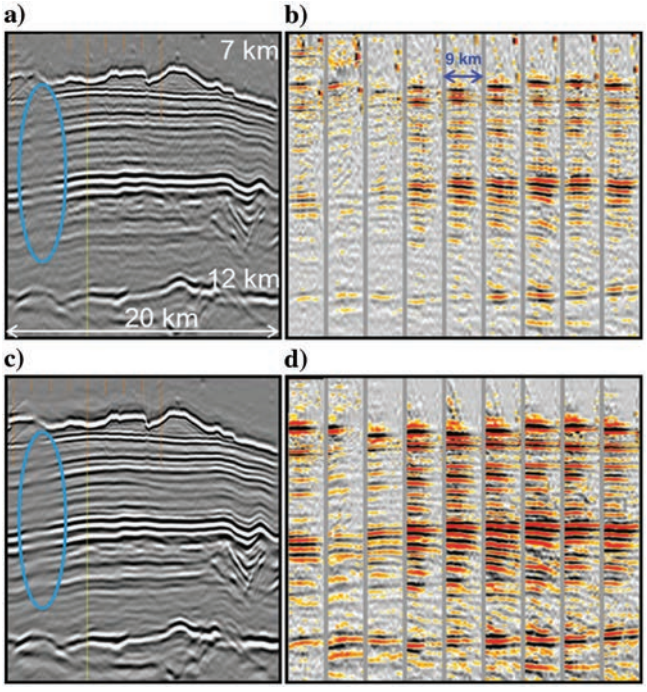

Figure 5. GOM field data example: (a) raw RTM stack image, (b) raw RTM surface-offset gathers, (c) LSRTM-CHF stack image, and (d) LSRTM-CHF surface-offset gathers. The orange lines in (a and c) mark the gather locations in (b and d).

Figure 5b shows raw RTM SOGs (m_0^{sog}) at locations indicated by the yellow lines in Figure 5a, and Figure 5d shows the same gathers after CHF (m^{sog}). We observed that SOGs after CHF have a higher S/N and more continuous subsalt events across all offsets while retaining the event curvatures. As counterintuitive as it seems, we may be able to use CHF SOGs to improve the velocity model, even though LSRTM assumes the velocity model is already correct. One possibility is to include CHF into key velocity model building steps, e.g., using the SOGs generated from CHF for better curvature picking and, in turn, better tomographic inversion. Of course, the computation of incorporating CHF in velocity estimation can be costly.

Figure 5c shows the stack image after CHF. The image has more balanced amplitudes and fewer migration artifacts compared with the raw stack image in Figure 5a. Note that events in the light blue circle were not well-imaged by RTM, possibly due to velocity errors and/or inaccurate salt interpretation. As a result, CHF was unable to fully recover the amplitude dimming.

Figure 6a shows a stratal slice of a reservoir surface. The amplitude pattern extracted from the raw RTM image appears rather random due to irregular illumination and migration artifacts. Figure 6b shows the same stratal slice after CHF. We observed that the higher amplitudes are clustered toward a structural high (depth contours indicated by the black curves in Figure 6). The red curves in Figure 6c show our interpretation of a subsalt channel based on the CHF image.

Discussion

Using SEAM I synthetic data and a GOM field data set, we demonstrated that image-domain single-iteration and

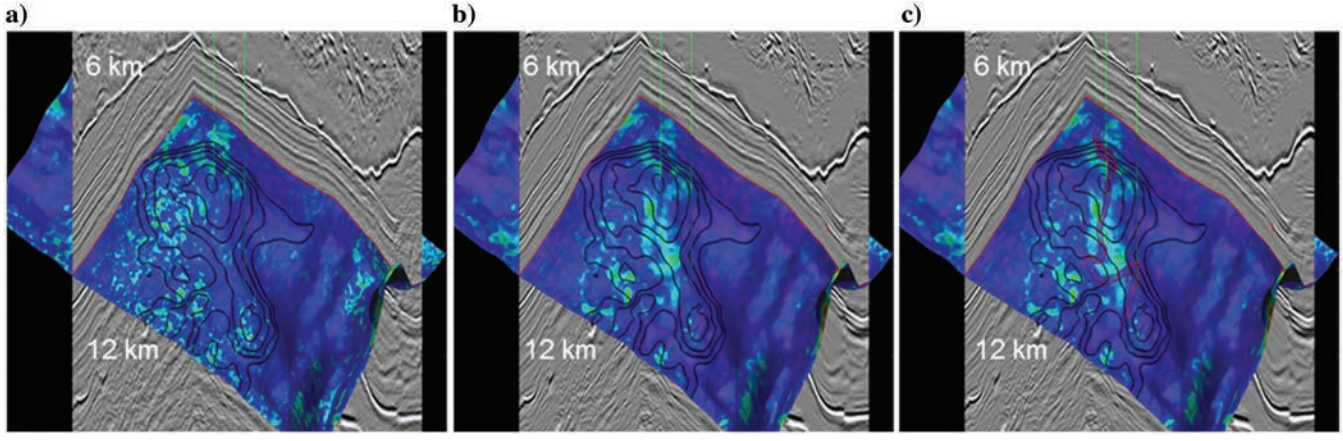

Figure 6. The GOM field data example: (a) stratal slice of raw RTM image (green, high amplitude; purple, low amplitude), (b) stratal slice of LSRTM-CHF image, and (c) stratal slice of LSRTM-CHF image overlaid with our interpretation of subsalt channel (red curves). The black curves are the reservoir horizon contours, and the vertical green lines indicate three wells with the only good well in the middle.

data-domain iterative LSRTM methods can reduce uneven subsalt amplitudes. Some consistent observations from both tests are as follows: (1) Single-iteration methods, including PSF and CHF, are far more computationally efficient than iterative LSRTM, (2) CHF images are cleaner than those from iterative LSRTM, and (3) iterative LSRTM has a slow convergence rate with migration noise and artifacts increasing with each iteration. Next, we try to explain some of these observations and propose possible ways to improve iterative LSRTM.

Some notes on CHF

Compared with Guitton's approach, CHF takes the advantage of the curvelet transform that decomposes seismic events into different orientations and frequency scales and therefore better handles frequency- and angle-dependent illumination patterns. Compared with PSF approaches, matching-filter methods such as CHF deconvolve a demigration/migration image (m_1) from the original image (m_0). The image used for the deconvolution is the weighted stack of impulse responses for all image points within a given spatial window. This means that CHF is inherently more stable than PSF deconvolution, which deconvolves a point-wise impulse response. This also means that it may not be able to fully compensate for the amplitude distortion that is modeled in the demigration/migration image. In addition, many other factors, such as nonfocusing due to velocity error and transmission loss, and elastic effects that cannot be addressed by methods using acoustic Born modeling, can prevent CHF from giving the correct amplitude. Therefore, at best, CHF can only produce a better amplitude response than the raw migration.

CHF results are usually cleaner than those from other methods. This is because (1) CHF applies matching filters on RTM SOGs instead of RTM stacks; thus, it has a better likelihood of attenuating migration artifacts that are inconsistent with offsets; (2) CHF is relatively insensitive to velocity error, inaccurate modeling algorithms, inaccurate source wavelet, and noise in the input data; and (3) the curvelet transform is sparse, and thus it can implicitly filter out random noise.

The PSF approach approximates the inverse of the Hessian matrix by a round-trip demigration/migration using a point-diffractor reflectivity model, whereas the CHF approach achieves the same round-trip effect using a migrated image as the reflectivity model. Theoretically, this round-trip demigration/migration can give the same illumination information for any reflectivity model (i.e., one can even use random noise as the reflectivity model). However, in practice, we found that using the migrated image as the reflectivity model serves as an image guide for random noise attenuation during the filter design in the curvelet domain. Furthermore, we observed that using a cleaner image with more balanced amplitudes as the reflectivity model gives better results in terms of illumination compensation and noise reduction.

As mentioned previously, CHF is performed in overlapping 3D spatial windows. Each window needs to be large enough for a stable filter derivation. However, a small spatial window is preferred to better honor any local variations in the Hessian matrix. This means that migration artifacts and illumination patterns on a large scale may not be well-handled by CHF. In theory, iterative LSRTM that is based on full-window global minimization does not have this limitation.

Some notes on iterative LSRTM

Theoretically, iterative LSRTM is more accurate in solving the inverse of the Hessian matrix, but it is inherently more sensitive to inaccurate modeling algorithms, velocity errors, incorrect source wavelets, and noise from residual multiples and other wave modes that cannot be modeled by acoustic Born modeling. To date, iterative LSRTM has not been widely used for subsalt imaging primarily for two reasons that stem from large discrepancies between the recorded data and acoustic Born-modeled data: (1) It is computationally expensive because of its slow convergence rate (if it converges at all), and (2) it creates false images or artifacts to explain some of the events in the input data that cannot be modeled by acoustic Born modeling.

One way to speed up iterative LSRTM is to use data encoding (Dai et al., 2014). However, the trade-off between efficiency and image quality can be highly dependent on the acquisition geometry and structural complexity. Another option is to precondition the gradient using PSFs or inverse Hessian filters (Huang et al., 2016). To reduce artifacts, a sparse transform can be used to regularize the gradient or the total image (Dutta et al., 2016). Encouraged by its performance on illumination compensation and noise reduction, we believe CHF may be a good candidate to precondition iterative LSRTM to improve convergence rate and reduce migration noise.

Conclusion

The performance of LSRTM is largely limited by the quality of the raw RTM image. It is very difficult, if not impossible, for any LSRTM method to recover subsalt events and structures that are completely missing on the raw RTM image. The absence of subsalt events on the raw RTM image can arise from a combination of factors, such as very low or no illumination, severe noise contamination, or an inaccurate velocity model. In subsalt imaging, a high-quality input data set not only provides better subsalt illumination and noise attenuation, it is also conducive to better velocity model derivation. Naturally, using a good input data set can increase the chances of success of LSRTM. A case in point is the advent of full-azimuth acquisition in the GOM, which has not only led to better subsalt illumination and noise cancellation but also produced higher fidelity velocity models than would be obtained from a wide-azimuth data set.

LSRTM has shown promising results in subsalt imaging. It improves the amplitude response and reduces migration artifacts for stacked images and gathers by compensating for irregular illumination due to complex overburdens and acquisition footprints. This can also

potentially benefit subsalt quantitative interpretation and time-lapse imaging. Through additional synthetic and field data trials, the subsalt imaging community will continue to improve the algorithms and turn more of the possible benefits of LSRTM into reality.

Acknowledgments

We thank SEG for the SEAM I 3D model and CGG for permission to publish this work. We also thank B. Bai for the stratal slices and A. Gomes, Z. Zhang, T. Huang, and R. Huang for their helpful discussions, and Y. Zhang, L. Duan, A. Khalil, Y. Xie, D. Trad, and numerous other CGG colleagues for their previous research on least-squares migration.

References

Baysal, E., D. Kosloff, and J. Sherwood, 1983, Reverse-time migration: Geophysics, **48**, 1514–1524, doi: 10.1190/1.1441434.

Claerbout, J. F., 1992, Earth soundings analysis: Processing versus inversion: Blackwell Scientific Publications.

Dai, W., Y. Huang, and G. T. Schuster, 2013, Least-squares reverse time migration of marine data with frequency-selection encoding: Geophysics, **78**, no. 4, S233–S242, doi: 10.1190/geo2013-0003.1.

Dai, W., K. Jiao, D. Coles, and R. T. Coates, 2014, Least-squares reverse-time migration with statistical sampling: 76th Annual International Conference and Exhibition, EAGE, Extended Abstracts, doi: 10.3997/2214-4609.20141162.

Dong, S., J. Cai, M. Guo, S. Suh, Z. Zhang, B. Wang, and Z. Li, 2012, Least-squares reverse time migration: Towards true amplitude imaging and improving the resolution: 82nd Annual International Meeting, SEG, Expanded Abstracts, doi: 10.1190/segam2012-1488.1.

Dutta, G., C. Agut, M. Giboli, and P. Williamson, 2016, Least-squares reverse time migration with Radon preconditioning: 86th Annual International Meeting, SEG, Expanded Abstracts, 4198–4203.

Etgen, J., S. Gray, and Y. Zhang, 2009, An overview of depth imaging in exploration geophysics: Geophysics, **74**, no. 6, WCA5–WCA17, doi: 10.1190/1.3223188.

Fletcher, R. P., D. Nichols, R. Bloor, and R. T. Coates, 2016, Least-squares migration — Data domain versus image domain using point spread functions: The Leading Edge, **35**, P159–P162.

Giboli, M., R. Baina, L. Nicoletis, and B. Duquet, 2012, Reverse time migration surface offset gathers, Part 1: A new method to produce 'classical' common image gathers: 82nd Annual International Meeting, SEG, Expanded Abstracts, doi: 10.1190/segam2012-1007.1.

Guitton, A., 2004, Amplitude and kinematic corrections of migrated images for nonunitary imaging operators: Geophysics, **69**, 1017–1024, doi: 10.1190/1.1778244.

He, K., J. Sun, and X. Tang, 2013, Guided image filtering: IEEE Transactions on Pattern Analysis and Machine Intelligence, **35**, 1397–1409, doi: 10.1109/TPAMI.2012.213.

Hu, J., G. T. Schuster, and P. A. Valasek, 2001, Poststack migration deconvolution: Geophysics, **66**, 939–952, doi: 10.1190/1.1444984.

Huang, W., P. Deng, and H. W. Zhou, 2016, Least-squares reverse time migration with Hessian preconditioning: 86th Annual International Meeting, SEG, Expanded Abstracts, 4193–4197.

Lecomte, I., 2008, Resolution and illumination analyses in PSDM: A ray-based approach: The Leading Edge, **27**, no. 5, 650–663, doi: 10.1190/1.2919584.

Nemeth, T., C. Wu, and G. T. Schuster, 1999, Least-squares migration of incomplete reflection data: Geophysics, **64**, 208–221, doi: 10.1190/1.1444517.

Rickett, J., A. Guitton, and D. Gratwick, 2001, Adaptive multiple subtraction with non-stationary helical shaping filters: 63rd Annual International Conference and Exhibition, EAGE, Extended Abstracts, P167.

Rickett, J. E., 2003, Illumination-based normalization for wave equation depth migration: Geophysics, **68**, 1371–1379, doi: 10.1190/1.1598130.

Sacchi, M. D., 1997, Reweighting strategies in seismic deconvolution: Geophysical Journal International, **129**, 651–656, doi: 10.1111/j.1365-246X.1997.tb04500.x.

Schuster, G. T., 1993, Least-squares crosswell migration: 63rd Annual International Meeting, SEG, Expanded Abstracts, 110–113, doi: 10.1190/segam2012-1425.1.

Tang, Y., 2008, Wave-equation Hessian by phase encoding: 78th Annual International Meeting, SEG, Expanded Abstracts, 2201–2205.

Tarantola, A., 1987, Inverse problem theory: Methods for data fitting and model parameter estimation: Elsevier Science Publishing Company.

Wong, M., S. Ronen, and B. Biondi, 2011, Least-squares reverse-time migration/inversion for ocean bottom data: A case study: 81st Annual International Meeting, SEG, Expanded Abstracts, 2369–2373, doi: 10.1190/1.3627684.

Zeng, C., S. Dong, and B. Wang, 2014, Least-squares reverse time migration: Inversion-based imaging toward true reflectivity: The Leading Edge, **33**, 962–968, doi: 10.1190/tle33090962.1.

Zhang, Y., L. Duan, and Y. Xie, 2013, A stable and practical implementation of least-squares reverse time migration: 83rd Annual International Meeting, SEG, Expanded Abstracts, 3716–3720, doi: 10.1190/segam2013-0577.1.

Zhang, Y., and H. Zhang, 2009, A stable TTI reverse time migration and its implementation: 79th Annual International Meeting, SEG, Expanded Abstracts, 2794–2798, doi: 10.1190/1.3255429.

Biographies and photographs of the authors are not available.